

Subscriber access provided by THE OHIO STATE UNIVERSITY LIBRARIES

Article

Reduced dislocation introduction in III-V/Si heterostructures with glide-enhancing compressively-strained superlattices

Jacob T Boyer, Ari N. Blumer, Zak H. Blumer, Daniel L. Lepkowski, and Tyler J Grassman

Cryst. Growth Des., Just Accepted Manuscript • DOI: 10.1021/acs.cgd.0c00992 • Publication Date (Web): 15 Sep 2020

Downloaded from pubs.acs.org on September 15, 2020

Just Accepted

"Just Accepted" manuscripts have been peer-reviewed and accepted for publication. They are posted online prior to technical editing, formatting for publication and author proofing. The American Chemical Society provides "Just Accepted" as a service to the research community to expedite the dissemination of scientific material as soon as possible after acceptance. "Just Accepted" manuscripts appear in full in PDF format accompanied by an HTML abstract. "Just Accepted" manuscripts have been fully peer reviewed, but should not be considered the official version of record. They are citable by the Digital Object Identifier (DOI®). "Just Accepted" is an optional service offered to authors. Therefore, the "Just Accepted" Web site may not include all articles that will be published in the journal. After a manuscript is technically edited and formatted, it will be removed from the "Just Accepted" Web site and published as an ASAP article. Note that technical editing may introduce minor changes to the manuscript text and/or graphics which could affect content, and all legal disclaimers and ethical guidelines that apply to the journal pertain. ACS cannot be held responsible for errors or consequences arising from the use of information contained in these "Just Accepted" manuscripts.

Reduced Dislocation Introduction in III-V/Si

Heterostructures with Glide-Enhancing

Compressively-Strained Superlattices

Jacob T. Boyer¹, Ari N. Blumer^{1,2}, Zak H. Blumer¹, Daniel L. Lepkowski³, and Tyler J. Grassman^{1,2,3}*

¹Department of Materials Science and Engineering

The Ohio State University

105 W. Woodruff Ave, Columbus, OH 43210, USA

²Center for Electron Microscopy and Analysis

The Ohio State University

1305 Kinnear Road, Suite 100, Columbus, OH 43212

³Department of Electrical and Computer Engineering

The Ohio State University

2015 Neil Ave, Columbus, OH 43210

Keywords: III-V/Si, dislocations, superlattices, TDD, GaAsP

ABSTRACT The novel use of a GaAs_yP_{1-y}/GaP compressively-strained superlattice (CSS) to provide enhanced control over misfit dislocation (MD) evolution and threading dislocation density

(TDD) during GaP/Si metamorphic heteroepitaxy is demonstrated. Insertion of the CSS just after critical thickness, and thus prior to substantial dislocation introduction, is found to yield significantly reduced TDD in relaxed, 500 nm thick, n-type GaP/Si versus comparable control samples. The impact of CSS period count on average TDD and the overall dislocation network morphology was examined, supported by quantitative microstructural characterization, revealing a nearly 20^{\times} relative TDD reduction (to $2.4 \pm 0.4 \times 10^6$ cm⁻²) with a 3-period CSS structure. A similarly low TDD ($3.0 \pm 0.6 \times 10^6$ cm⁻²) is maintained when the resultant n-GaP/Si virtual substrate is used for the growth of a subsequent n-type GaAs_{0.75}P_{0.25}-terminal GaAs_yP_{1-y} step-graded metamorphic buffer. Although the physical mechanism for TDD reduction provided by these structures is not yet entirely understood, this initial work suggests that enhanced glide dynamics of MDs at or within the CSS placed early in the growth leads to a reduction in the total number of dislocations introduced overall, as opposed to annihilation-based reduction that occurs in conventional strained-layer superlattice dislocation filter approaches.

1. Introduction

High-quality, epitaxially-integrated III-V/Si heterostructures and virtual substrates have been sought for decades to reduce III-V device fabrication costs and to expand the functionality of both III-V and Si platforms. Integrated III-V/Si materials systems have potential relevance to a wide array of semiconductor electronic and photonic technologies, including monolithic III-V/Si multijunction photovoltaics (PV) that employ the underlying Si as an active subcell.

Development of high-quality III-V/Si materials tailored to these "Si-based tandems" is the

primary motivation of the work herein, but the problem addressed, and solution thereof, is of much broader interest and applicability.

Recent years have witnessed multiple demonstrations of monolithic epitaxial III-V/Si solar cells, including GaAs_{0.75}P_{0.25}/Si dual-junction¹⁻³ and Ga_{0.51}In_{0.49}P/GaAs/Si triple-junction designs.⁴ Enabled by foundational work to mitigate the nucleation-related defects inherent to heterovalent GaP/Si integration,⁵⁻⁸ a common integration pathway employed for these (and similar) PV-oriented heteroepitaxial III-V/Si systems is via metamorphic GaAs_yP_{1-y}/GaP/Si compositional grading, typically in the form of step-graded buffers (SGBs). The optically-transparent (to photons transmitted by the upper junctions) SGB structure serves to controllably bridge the lattice mismatch between Si and the III-V upper junction composition(s). Nonetheless, while these early prototypes highlight the promise of this integrated materials system, the ultimate potential of the architecture is still yet to be fully realized due to, in large part, excessive threading dislocation (TD) content in the metamorphic III-V active layer(s).^{2,9-11}

A significant amount of work has focused on the minimization of threading dislocation density (TDD) within the metamorphic $GaAs_yP_{1-y}/Si$ system. Careful optimization of the epitaxial growth has, for example, led to the demonstration of high-quality, p-type $GaAs_{0.75}P_{0.25}/GaAs_yP_{1-y}/Si$ with TDD as low as 4×10^6 cm⁻².^{12,13} However, to yield the low-resistance band alignment at the III-V/Si interface needed to enable a series-connected, two-terminal tandem solar cell, ^{2,3,14,15} it is generally recognized that an n-type interface is necessary — i.e. n-type III-V materials and an n-type Si surface (e.g. an n⁺-Si emitter layer). And yet, progress toward TDD reduction in the n-type polarity metamorphic structures significantly lags that of the p-type. At present, limitations in this pursuit appear to stem almost entirely from high starting TDD in the initial n-GaP/Si virtual substrate. The relative difficulty in optimization may

be related to the difference in intrinsic dislocation glide velocities for different doping types. For example, in GaAs at 10^{18} cm⁻² doping concentrations, β dislocations in n-type exhibit $\sim 100 \times$ slower glide than in p-type. ¹⁶ Although similarly complete datasets do not appear to be available for GaP, the general dislocation glide behavior trends are found to be similar to GaAs, though overall the dislocation glide velocities are roughly two orders of magnitude slower in GaP. ¹⁷

In other III-V/Si systems, like GaAs/Si, TDD reduction has often been achieved using strained-layer superlattice (SLS) based dislocation filter layers (DFLs). Traditionally, such DFLs are grown on epilayers with high pre-existing TDD, where the alternating compressive- and tensile-strained interfaces, often in conjunction with thermal cycled annealing, 18,19 yields significantly enhanced dislocation glide activity that promotes annihilation reactions between proximal defects. 20 However, DFLs are generally found to be most effective when used in high-TDD scenarios, as below some threshold TDD (\sim 1×10 7 cm $^{-2}$) the average distance between TDs becomes too large to support continued annihilation reactivity. 21,22 On the other hand, thick-period SLS structures have also been shown to enable dislocation control and/or reduction on ultra-low-TDD (\leq 1×10 4 cm $^{-2}$) GaAs substrates, where annihilation reactions will be statistically rare, by promoting and enhancing dislocation glide all the way out to the wafer edges. 23,24

To this end, we hypothesize that a similar approach to enhance dislocation glide within n-GaP may help to prevent the introduction of excess TDD during n-GaP/Si heteroepitaxy. We have thus investigated the use of compressively-strained superlattices (CSS), employed within the n-GaP/Si growth structure, to provide enhanced dislocation glide dynamics and lower resultant TDD. Unlike traditional DFLs, these CSS structures are inserted early within the GaP/Si growth, just after critical thickness. At this point, dislocation nucleation has already begun, but has not vet proceeded to a substantial degree (TDD \sim 7×10⁴ cm⁻²). The design of the CSS structure here

is intended to interact with the dislocation loops as they form at the surface and glide down toward the strained interface(s), where the increased localized stresses are expected to enhance the dislocation glide velocities and promote more efficient MD elongation. This process would allow the epilayer to relax more efficiently, thereby minimizing the total number of dislocations needed to be introduced.

The initial investigations reported here show that these CSS structures do indeed yield significant TDD reduction of nearly 20× in relaxed, thick (500 nm) *n*-GaP/Si samples versus those without them. Comparing control and CSS-containing samples, at an equivalent TDD, the CSS relaxes more of the epilayer strain; at an equivalent relaxation, the CSS introduces far fewer dislocations. Applicability of the resultant low-TDD virtual substrates toward subsequent growth of metamorphic *n*-GaAs_yP_{1-y} SGBs is also demonstrated, resulting in *n*-type GaAs_{0.75}P_{0.25}/Si with TDD among the lowest reported to date and equivalent to *p*-type results.¹²

2. Methods

All of the III-V/Si heteroepitaxial structures discussed herein were grown via metalorganic chemical vapor deposition (MOCVD) in a 3×2 Aixtron close-coupled showerhead reactor with *in-situ* monitoring by a kSA ICE reflectance/pyrometry system. Precursors used were silane (SiH₄), triethylgallium (TEGa), *tert*-butylphosphine (TBP), arsine (AsH₃), and phosphine (PH₃). Thin (50 nm) *n*-GaP/Si templates were grown on 4" Si(001) substrates offcut 2° toward [110] following our previously reported methods.^{2,6} These wafers were then cleaved into quarters for regrowth of the different test structures, providing a nominally identical starting point for every case.

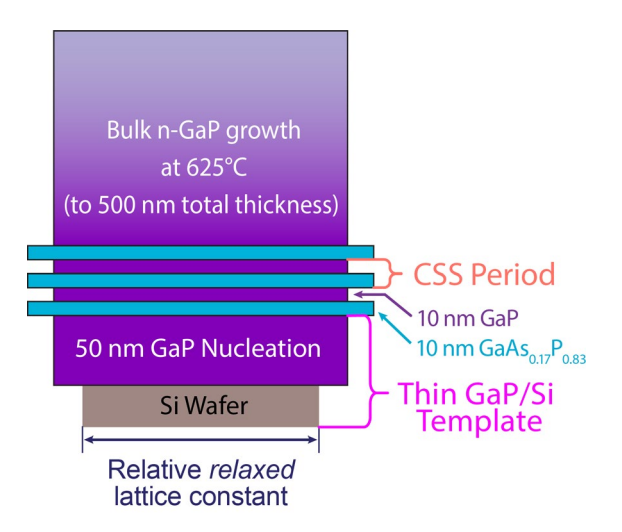


Figure 1. Schematic diagram of a 3-period CSS structure. Equilibrium lattice constants are depicted by the width of each material layer (not to scale).

Figure 1 presents a schematic depiction of the CSS test structures produced in this study.

Samples with 1-, 3-, and 5-period superlattices, as well as control samples with no CSS ("0-period"), were grown on the thin *n*-GaP/Si templates without homoepitaxial GaP regrowth. Each CSS period consists of a layer of *n*-GaAs_{0.17}P_{0.83} and a layer of *n*-GaP, which provides an enhanced local interfacial strain of ~1.13% at growth temperature (i.e. 0.66% from GaAs_{0.17}P_{0.83}/GaP on top of the 0.47% from GaP/Si); these higher stresses should nominally increase the local dislocation glide velocity. Additionally, it is assumed that the higher As fraction (nominally 17%), will result in higher glide velocity, following the general aforementioned trend between GaAs and GaP. It is possible that solid solution strengthening (alloy hardening) may counteract this trend, but there is insufficient reported evidence at present to make a conclusive determination either way, ^{26–28} and it is expected that the higher local stresses should nonetheless still provide enhanced glide. Because a material with equivalent tensile strain to fully balance the GaAs_{0.17}P_{0.83} layers was not readily available (and thus GaP

was used), the CSS layers were kept relatively thin to minimize the total compressive stress and risk of runaway dislocation introduction. As such, the individual GaAs_{0.17}P_{0.83} layers were grown to 10 nm each, below their nominal Matthews-Blakeslee critical thickness (assuming, for simplicity, GaAs_{0.17}P_{0.83} with respect to GaP and using equilibrium lattice constants for each);²⁴ the maximum total CSS thickness considered was 100 nm (for the 5-period structure). Given the dynamic, compressive strain across the entire structure, it is likely that the critical thickness of the whole stack with respect to GaP is surpassed, allowing MDs to elongate along the interface(s) of the CSS.

All films up to a total nominal thickness of 500 nm (including thin *n*-GaP/Si template, CSS structures, and *n*-GaP overgrowth) were produced under the same conditions, using a substrate temperature of 625°C and growth rate of ~0.5 μm/hr. To investigate the state of relaxation and dislocation evolution at an intermediate post-CSS thickness, a 5-period CSS sample with only 50 nm additional *n*-GaP overgrowth (thus a total III-V thickness of 200 nm) was also produced. Intermediate control samples, without CSS, with thicknesses of 100 nm and 250 nm were also produced.

To examine the impact of the CSS structure on residual TDD in subsequent metamorphic buffers, additional growths were also performed. Using the 500 nm thick n-GaP/Si structures as virtual substrates (both 0-period control and 3-period CSS versions), n-GaAs_yP_{1-y} step-graded buffers (SGBs) were grown at $675 - 725^{\circ}$ C and $2.25 \,\mu$ m/hr. The SGBs employed nominal 3% As fraction steps and a misfit grading rate of either 0.5 or $1.0\%/\mu$ m for growth on the 0-period and 3-period CSS virtual substrates, respectively. All III-V epilayers in every structure were n-type doped (via SiH₄) to a target concentration of $1-2 \times 10^{18} \, \text{cm}^{-3}$.

The various epitaxial samples underwent both large-scale bulk and microscale defect-resolved structural characterization. High-resolution X-ray diffraction (XRD) reciprocal space mapping (RSM) was conducted in a Bede D1 triple-axis system using (224) and (004) reflections along both orthogonal <110> directions to assess relaxation/strain state of the epilayers. TDD was determined via direct counting from electron channeling contrast imaging (ECCI) micrographs collected with a Thermo Scientific Quattro SEM using conditions and methods described previously. To ensure statistically relevant quantification, large total area (~10,000 μm²) ECCI montages were composed, ensuring a raw count of at least 500 TDs per sample. Mean TDD and standard error across all micrographs is reported herein.

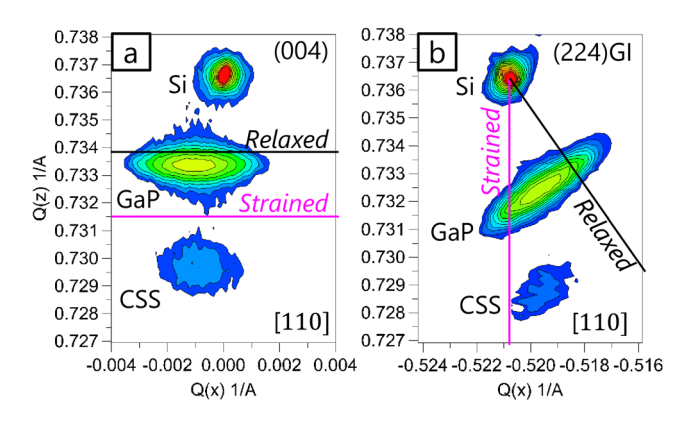


Figure 2. XRD RSMs of the 5-period CSS sample (500 nm) around (004) and (224) reflections of Si, taken with beam incident in the [110] direction. GaP and CSS (GaP/GaAs_{0.17}P_{0.83}) reflections are visible with intermediate relaxation states.

Table 1. Room temperature XRD relaxation values of bulk GaP and CSS layers, depending on incident direction. Note that the 1-period CSS structure was not sufficiently visible for analysis.

Epitaxial	XRD	500 nm				200 nm	100 nm
Layer	Zone	0-period	1-period	3-period	5-period	5-period	0-period
Bulk	[110]	98.1%	93.0%	95.8%	98.6%	60.7%	8.6%
GaP	[110]	53.4%	26.7%	49.5%	41.6%	7.8%	4.1%
CCC	[110]	n/a	n/a	55.7%	58.2%	39.1%	n/a
CSS	[110]	n/a	n/a	24.6%	19.1%	4.1%	n/a

3. Results and Discussion

3.1. Relaxation Analysis

All thick (500 nm) *n*-GaP/Si samples, both with and without CSS structures, exhibited smooth surface morphologies (via SEM), with little variance across specific sample designs. **Figure 2** shows representative (004) and (224) XRD RSMs taken from a 5-period CSS sample, with the beam incident along the [110] zone. Extracted relaxation values of GaP and CSS layers from all samples are provided in **Table 1**. In Figure 2, lines bounding the GaP peak, indicating both fully-relaxed and fully-strained GaP lattice constants, are given for reference. An additional peak corresponding to the average As composition of the CSS structure, ~9%, is found at the same inplane lattice constant as that of the surrounding partially-relaxed bulk GaP, which lies between the equilibrium lattice constants of GaP and Si. Taken as a whole, the CSS has roughly half the

relaxation of the bulk GaP, indicating that the individual GaAs_{0.17}P_{0.83} layers are fully strained with respect to the surrounding GaP. Similar XRD RSMs taken on all thick samples (500 nm total III-V thickness) indicate room temperature relaxation values of 93-99% and 27-53% for the [110] and [$\bar{1}$ 10] directions, respectively. No clear trends in relaxation versus CSS period count are observed, and thus any differences are likely the result of run-to-run variation. XRD RSMs taken on the intermediate (200 nm, 5-period) sample indicate that relaxation is 61% and 8% for the [110] and [$\bar{1}$ 10] directions, respectively. The 100 nm 0-period (control) sample is mostly strained, with 9% and 4% relaxation in the [110] and [$\bar{1}$ 10] directions, respectively. The asymmetry in relaxation observed throughout all of the structures is likely due to the well-studied anisotropy in α and β dislocation glide velocities. ¹⁶

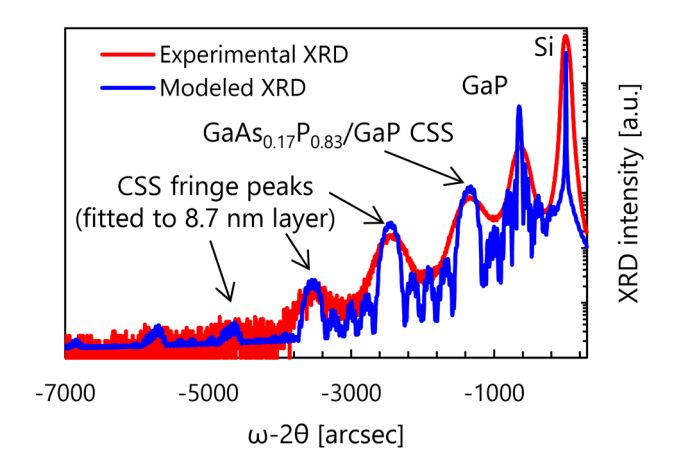


Figure 3. XRD (004) ω -20 scan of the 5-period CSS sample (500 nm) showing higher order peaks arising from the CSS structure. A superlattice period thickness of 8.7 nm was found by fitting of the fringe peaks.

Fringe peaks due to the CSS structure were also observed but are too weak to clearly visualize in the triple-axis RSMs. Instead, **Figure 3** presents a double-axis (004) ω -2 θ scan of the same

sample and geometry as Figure 2. The superlattice nature of the CSS is clearly signified by the presence of multiple higher order peaks. Analysis of the superlattice fringe peaks was performed using Bede Rocking-Curve Analysis by Dynamical Simulation software (Bede RADS). The peak spacing was fit to a superlattice layer thickness of 8.7 nm, which reasonably agrees with the 10 nm experimental target. The discrepancy is likely due to a slight miscalibration of the growth rate for at least one of the layer constituents, but is not critical for this initial demonstration.

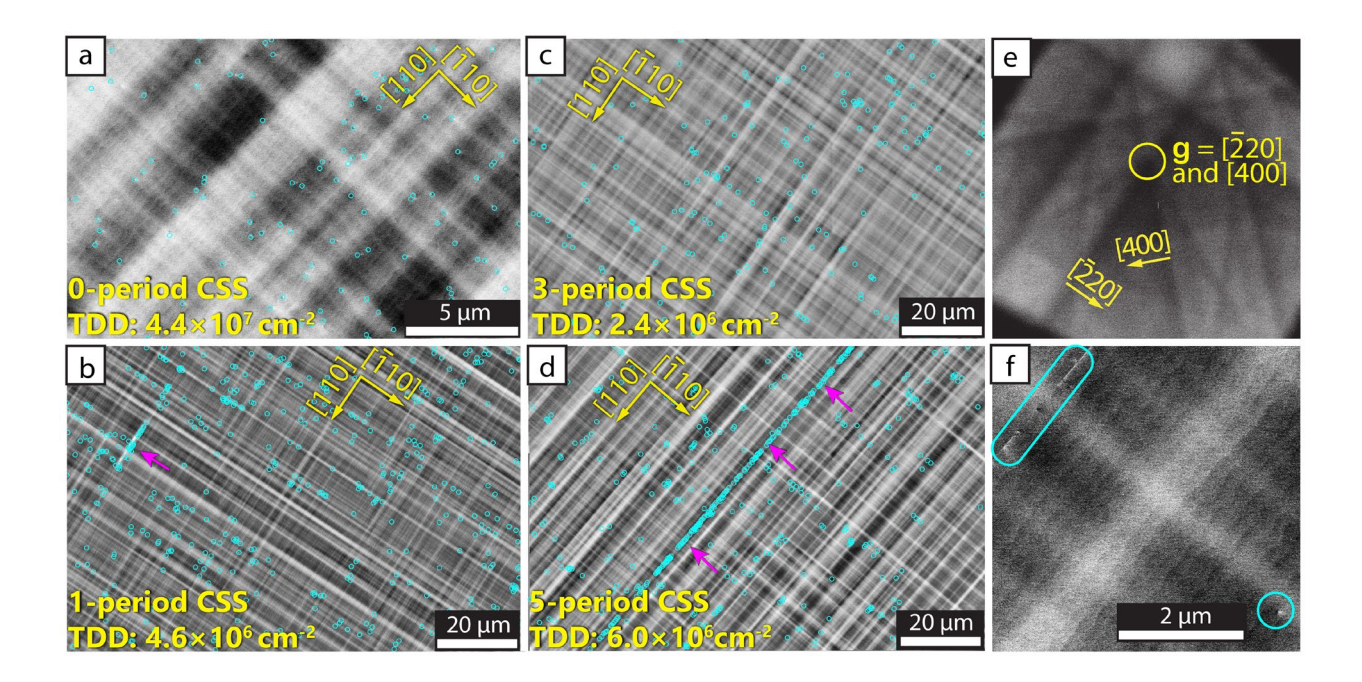


Figure 4. ECCI micrographs of thick CSS virtual substrates containing (a) no CSS (control) and (b) 1-, (c) 3-, and (d) 5-period CSS structures with threads marked by cyan circles. (e) Depicts the electron channeling pattern used to select $g = [2\bar{2}0]$ and [400] that was used for all imaging. (f) shows a magnified view of TDs and pile-ups. Due to higher TDD of the control, the scale of (a) is a single higher-magnification image, whereas (b)-(d) are multi-image montages. All micrographs were adjusted for clarity using FFT noise reduction filtering.

3.2. Impact of CSS Structures on n-GaP/Si TDD

While CSS period count does not appear to affect relaxation state, drastic differences in dislocation content were observed, revealing a clear impact resulting from the CSS insertions. **Figure 4(a-d)** presents ECCI image examples collected from all four test cases. To ensure visibility (contrast) of all potential TDs, images were taken at a diffraction condition defined by the intersection of $\mathbf{g} = [\overline{2}20]$ and [400], as shown in Figure 4(e). Although the features can be somewhat difficult to see in the lower magnification images given in Figure 4(a-d), these large-area images provide statistically accurate representation; each individual TD positions is indicated by a circle. Additionally, Figure 4(f) provides a high-magnification example of an individual TD and a cluster within a pile-up. Note also that the 0-period control sample is shown at a higher magnification due to its significantly higher TDD (and thus smaller TD spacing). Extracted numerical TDD values, based on these (and additional) ECCI micrographs are summarized in **Figure 5.**

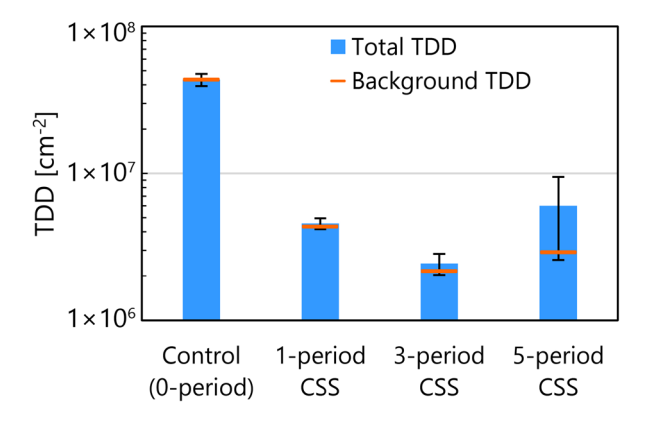


Figure 5. Total TDD and background TDD extracted from ECCI micrographs for all CSS structures and control.

The 500 nm n-GaP/Si 0-period control sample, Figure 4(a), was found to possess a TDD of $4.4 \pm 0.4 \times 10^7$ cm⁻². Because the growth conditions for the thick "bulk" n-GaP are not necessarily fully optimized, this baseline TDD is likely somewhat higher than what should ultimately be achievable with this simple structure. However, as previously noted, the intrinsic dislocation dynamics limitations of n-GaP make it unlikely that the same low TDD values previously demonstrated in p-GaP/Si¹³ could be achieved here. Nonetheless, samples grown with only a single n-GaAs_{0.17}P_{0.83}/GaP CSS period inserted, and all else kept the same, result in an order of magnitude reduction to $4.6 \pm 0.4 \times 10^6$ cm⁻². With a 3-period CSS structure, Figure 4(c), another $2 \times$ reduction is achieved (nearly $20 \times$ versus the control), yielding a TDD of $2.4 \pm 0.4 \times 10^6$ cm⁻², the lowest demonstrated in this present study.

Interestingly, the 5-period CSS structure was found to reverse this downward trend, yielding a $2.5\times$ overall higher TDD of $6.0\pm3.0\times10^6$ cm⁻² than the 3-period version. This is a direct consequence of the increased prevalence of TD pile-up lines lying along the <110> directions, like that indicated by the arrows in Figure 4(b) and 4(d). These features were found to have a local TDD of $\sim 3\times10^8$ cm⁻², substantially higher than the background density. As such, for each case, Figure 5 gives both the extracted total TDD, as well as uniform background TDD obtained by subtracting the TDs found in pile-ups. To that end, the 5-period background TDD of $2.9\pm0.2\times10^6$ cm⁻² is actually very similar to that of the 3-period case. However, when included in the analysis, the $\sim 3\times$ increase in pile-ups for the 5-period case relative to the others effectively accounts for both the significant overall average TDD increase and the spatial variance (i.e. pile-up versus background) that produces the wider associated error bar in Figure 5.

For further investigation of the TDD evolution during growth, as well as the functional mechanism of the CSS structure, the intermediate thickness (200 nm total III-V) 5-period CSS n-GaP/Si sample (referred to as 'intermediate 5-period' hereafter) was also analyzed via ECCI, as presented in **Figure 6**. Here, single diffraction conditions of $\mathbf{g} = [\bar{2}20]$ and [220] were used to individually image the misfit dislocation (MD) networks with line directions $\mathbf{u} = [110]$ (Figure 6a) and $[\bar{1}10]$ (Figure 6b), respectively. MDs, rather than TDs, are observed due to this film being thinner than the 500 nm GaP films, wherein the MDs are too deep to be readily visible. 30,32 Here, MDs appear as long bright or dark lines depending on their respective Burgers vector. The MD lines are typically found at this point to be 100's of micrometers long, but endpoints are occasionally observed, corresponding to where the dislocation line bends upward away from the interface to form a TD segment, which is not easily visible in low magnification micrographs against the strong MD contrast. 25,33 Counting these endpoints over a large area ($\geq 10,000 \ \mu m^2$) yields an effective TDD of $9.1 \pm 0.4 \times 10^5 \ cm^{-2}$, intermediate to the TDD of the thin 50 nm template and the final 500 nm n-GaP/Si structure.

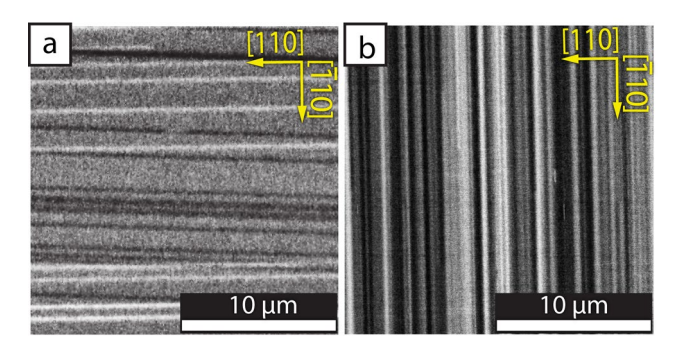


Figure 6. ECCI micrographs depicting MD arrays in a 5-period CSS sample with 50 nm GaP overgrowth using selective imaging via (a) $\mathbf{g} = [\overline{2}20]$ to image MDs with line direction $\mathbf{u} = [110]$ and (b) $\mathbf{g} = [220]$ to image MDs with line direction $\mathbf{u} = [\overline{1}10]$.

Considering that the TDD of the intermediate 5-period sample is more than an order of magnitude higher than the starting value of the 50 nm template (prior to the growth of the CSS itself), and more than $3\times$ lower than the final background TDD at 500 nm, it is likely that no significant conventional dislocation filtering (i.e. reduction down from a higher value) is occurring. That is, the TDD appears to show a strictly monotonic increase — 7×10^4 , 9×10^5 , and 3×10^6 cm⁻² at 50, 200, and 500 nm, respectively, as shown in **Figure 7**. The TDD trend for 50, 100, 250, and 500 nm thick control case samples is also presented, exhibiting a higher rate of dislocation introduction all around.

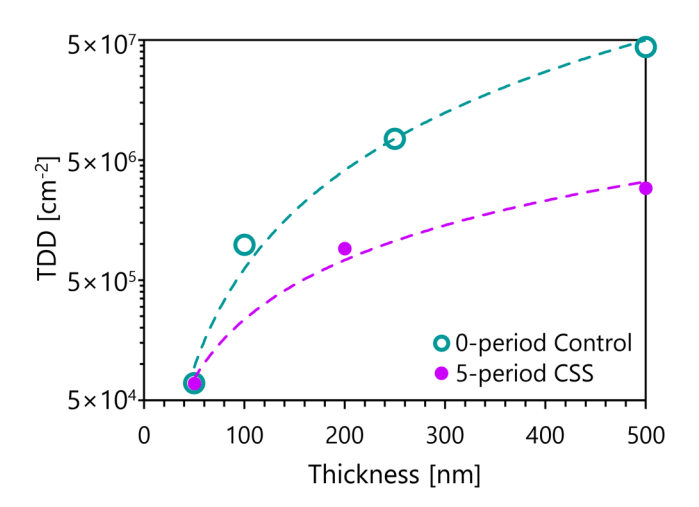


Figure 7. TDD trends with thickness for the 5-period CSS case and the 0-period (control) case. Power law trendlines are provided as a guide to the eye.

It might be expected that the significant stress introduced by the CSS itself would lead to an increased dislocation introduction rate, especially for the 5-period case. And yet, <30% of the final total (500 nm) TDD has actually been generated by the 200 nm intermediate point. This point is found to be equivalent in TDD to the 100 nm control sample, suggesting that the impact

of the extra stress has been somehow mitigated. The increase in TDD that would otherwise occur in the control sample throughout the 50 nm to 150 nm thickness range does not occur when the 5-period CSS structure is placed within this same region, despite the fact that it actually provides additional strain versus GaP alone. Thus, it is as though the 100 nm 5-period CSS structure itself is effectively "invisible" with respect to net dislocation introduction. While the intermediate 100 nm control and intermediate 5-period samples both reach the same TDD, the relaxation in the CSS case is found to be \sim 7× and \sim 2× greater for the [110] and [$\bar{1}$ 10] directions, respectively (see Table 1).

Although the exact TDD and relaxation as a function of growth time cannot be obtained, given a resultant population of $\sim 1 \times 10^6$ cm⁻² TDD in both cases, we can clearly conclude that the CSS enables more efficient relaxation overall than the n-GaP alone. The implication here is that the average total glide (i.e. MD line length) for the resident dislocations is higher due to the CSS. Taken together, these results suggest that insertion of the CSS structure yields TDD reduction by actually decreasing the total number of dislocations introduced into the system, unlike conventional DFL-type approaches, which actively reduce already-high TDD through annihilation reactions between existing dislocations.

Conclusive determination of such a mechanism is not straightforward, but consideration of the relaxation states and residual TDD of the various samples provides additional support. First, note that the density of MDs in the initial thin n-GaP/Si template — 3.5×10^4 cm⁻², assuming all dislocations have formed in the half loop geometry with two TDs per MD segment — is insufficient to provide the $\sim 100\% / 50\%$ ([110] / [$\bar{1}$ 10]) room temperature relaxation of the 0.37% misfit observed for all of the 500 nm total growths, even if all of these loops were to glide out to the sample edges.^{34–36} Following similar work, while adjusting for a surface half-loop

dislocation microstructure and including a circular correction factor,³⁷ we can estimate that to fully relax the area of the 4" wafer quarters employed in this study a minimum (i.e. geometrically necessary) MD density of $\sim 1 \times 10^5$ cm⁻², or $\sim 3 \times$ the template starting value, is needed.^{35,37}

While dislocation introduction of at least $3\times$ that of the starting template is necessary, the samples studied herein exhibit significantly higher levels of dislocation loop introduction beyond this minimum, geometrically necessary density. Using the TDD data in Figure 4 and 5, the 0-period (control) and 3-period CSS cases can be considered as the high- and low-TDD extremes, respectively. Both cases show an equivalent relaxation state, but with differing levels of excess dislocation introduction. The total observed differences in dislocation density versus the minimum, geometrically necessary density are $\sim 220\times$ and $\sim 12\times$, respectively; in both cases we can safely assume that the vast majority of the MDs do not run edge-to-edge. The magnitude of the strain relieved (relaxed) in a given direction, δ , can be determined as

$$\delta = \frac{\rho \cdot l \cdot b}{4},\tag{1}$$

where ρ is the TDD corresponding to the orthogonal MD lines (and thus provide a strain relief in the direction of δ), l is the average length of those lines, and b is the magnitude of their Burgers vector (in this case, for 60° dislocations). Therefore, given the equal relaxation state (relaxed epilayer strain relative to the total 0.37% GaP/Si misfit) of these two structures, but nearly 20^{\times} difference in dislocation density, the average length of the MDs in the 3-period structure — the majority of which we have already established are introduced after the CSS — must be significantly longer (by $\sim 20^{\times}$) than in the 0-period. Within a given <110> direction, the effective MD elongation rate, l, (which is twice the effective glide velocity assuming both MD ends are gliding) can be determined as

$$\dot{l} = 2\mathbf{v} = \frac{4\dot{\delta}}{\rho * b} \,, \tag{2}$$

where $\dot{\delta}$ is the strain relaxation rate, and v is the effective dislocation glide velocity acting on a mobile population of dislocations, ρ . Real Population of dislocations, ρ . Some estimates of strain relaxation rate for both the control and 5-period CSS cases can be obtained from the relaxation at 500 nm (at growth temperature) divided by the ~3200 s elapsed beyond critical thickness (~40 nm). Taking the overall relaxation rate in the $[\bar{1}10]$ direction (corresponding to the slower β dislocations) for both the control and 5-period CSS cases and, assuming equal populations of α and β dislocations, half the total TDD of the intermediate samples (the 250 nm control or the 200 nm 5-period CSS), effective glide velocities can be calculated, vielding $\sim 2 \times 10^{-7}$ m/s and $\sim 1 \times 10^{-6}$ m/s for the control and 5-period CSS cases, respectively. For simplicity, this calculation assumes that the TDD of these intermediate samples does not increase over time. However, as presented in Fig. 7, the TDD does actually increase beyond that of these intermediate samples, by around 3× for the CSS (5-period version, and thus likely less for the 3-period) and nearly 10× for the control; as such, the actual glide velocities are likely lower than these estimates, especially for the control. If we consider an average dislocation glide velocity of 2×10^{-7} m/s (i.e. the control case), then a total mobile TDD of 1.4×10⁷ cm⁻² (i.e. each directions has 7×10⁶ cm⁻² TDD, or 3.5×10⁶ cm⁻² complete dislocation loops) is necessary, at minimum, to fully relax the misfit of GaP/Si at growth temperature during the ~1 hour of growth. Similarly, if the glide velocity increases to 1×10⁻⁶ m/s (i.e. the CSS case), a total mobile TDD of 2.6×10⁶ cm⁻² would be required. Although the real relaxation behavior is much more dynamic than this simplistic analysis, it clear that for the control case, with dislocation glide velocities of around 1×10^{-7} m/s, the only reasonable pathway for effective relaxation is through the introduction of additional dislocations, whereas with the CSS this need is substantially reduced.

Because all growth conditions and final relaxation states were nominally identical, the difference in TDD can only be explained via roughly an order of magnitude enhancement in effective dislocation glide velocity in the 3-period CSS structure, and indeed in all CSS structure versions, versus the control. While many potential mechanisms — increased local stress to glide TDs, reduced dislocation blocking, multiple interfaces, etc. — could account for this enhancement, the observed initial and final states of relaxation and TDD necessitate that the overall extent of dislocation glide is enhanced as a result of the CSS. Given the slightly higher TDD versus that of the 3-period and 5-period (background) variants, it appears as though the glide enhancement is not as strong in the 1-period CSS case. Whether this is related to the number of strained interfaces or the total extra stress provided by the CSS layers, or even some other factor, is not yet known. Similarly, the impact of period thickness has not yet been explored.

Table 2. Residual TDD, measured via ECCI, in the GaAs_{0.75}P_{0.25}-terminal GaAs_yP_{1-y} graded buffer grown on control and CSS type GaP/Si virtual substrates.

Sample	Virtual Substrate	Terminal TDD		
	V II VIIII S II SVI II V	[×10 ⁶ cm ⁻²]		
A	500 nm GaP/Si, 3-period CSS	3.0 ± 0.6		
В	500 nm GaP/Si, no CSS (Control)	20.3 ± 2.4		
С	50 nm GaP/Si, no CSS	19.6 ± 4.3		

3.3. Application to n-GaAs_vP_{1-y}/Si Metamorphic Buffers

Next, the obvious question is whether the low TDD achieved in the *n*-GaP/Si CSS structures will support subsequent metamorphic growth for production of integrated devices, such as the previously discussed GaAs_{0.75}P_{0.25}/Si tandem solar cells. To this end, *n*-GaAs_yP_{1-y} step-graded buffers (SGBs) were grown on 500 nm thick, relaxed *n*-GaP/Si virtual substrates that either make use of a 3-period CSS structure (Sample A) or a 0-period control structure (Sample B). Growth was also performed directly on a thin, 50 nm pseudomorphic *n*-GaP/Si template (Sample C) as an additional level of control. TDD was then measured via ECCI at the terminal composition (GaAs_{0.75}P_{0.25}), the results from which are listed in **Table 2**. Note that Sample B was grown with a lower misfit grading rate of 0.5%/μm, whereas A and C were grown with a more aggressive grading rate of 1.0%/μm; the latter yield thinner buffers that help reduce the dynamic stresses induced during temperature changes.

The TDD of the two non-CSS cases are effectively identical at $\sim 2 \times 10^7$ cm⁻². For Sample B, this actually represents a $\sim 2 \times$ reduction versus the 4.4×10^7 cm⁻² of the 500 nm n-GaP/Si virtual substrate itself. Similarly, while the thin, pseudomorphic n-GaP/Si template starting TDD for Sample C is much lower (7×10^4 cm⁻²), separate test growths indicate that the excess strain introduced by the first SGB step (GaAs_{0.04}P_{0.96}) induces rampant dislocation introduction, yielding TDD of $> 5 \times 10^7$ cm⁻². Interestingly, in both cases, the terminal TDD of $\sim 2 \times 10^7$ cm⁻² suggests that the buffer itself is providing a small degree of dislocation filtering, similar to that achieved with traditional DFLs.^{21,22,39}

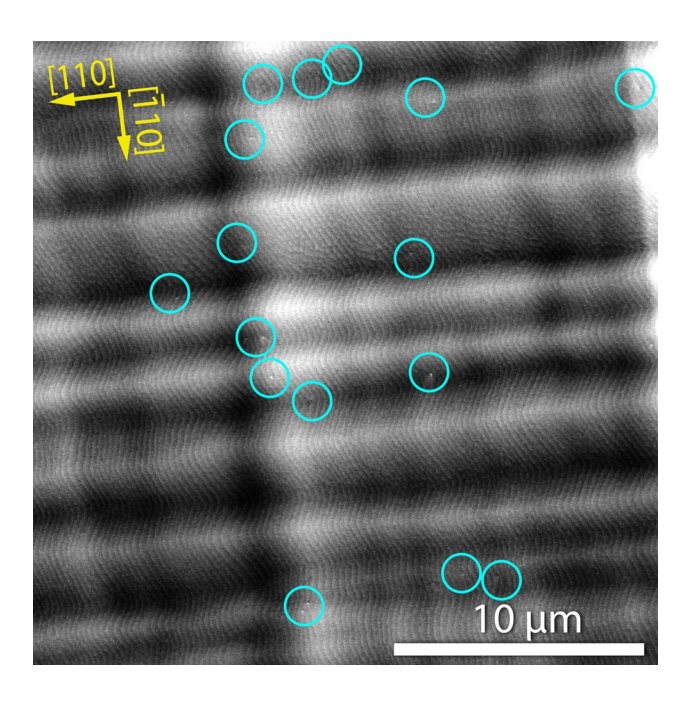


Figure 8. ECCI micrograph of GaAs_{0.75}P_{0.25} terminal layer of SGB structures grown on a virtual substrate with 3× CSS structure. TDs are marked with cyan circles.

In the case of the 3-period CSS structure (Sample A), the terminal TDD was drastically lower, $3.0 \pm 0.6 \times 10^6$ cm⁻², representing little to no increase (within the error range) from the virtual substrate starting point of $2.4 \pm 0.4 \times 10^6$ cm⁻². Despite the thinner, more aggressively graded SGB, this TDD, shown by the ECCI micrograph in **Figure 8**, is lower than even those reported for epitaxially-integrated GaAs_{0.75}P_{0.25}/Si that used thicker SGB's and all *p*-type material. As such, the 3-period CSS structure may be an excellent candidate to enable the production of low-TDD, high-performance GaAs_{0.75}P_{0.25}/Si solar cell structures, or any other III-V/Si, in general.

4. Conclusion

The insertion of 1-, 3-, and 5-period n-GaAs_{0.17}P_{0.83}/GaP compressive superlattice structures (CSS) just after critical thickness within thick (500 nm), fully-relaxed n-GaP/Si heteroepitaxial growths was found to yield significantly reduced TDD versus control samples with no CSS. TDD reductions of at least $5\times$, and up to nearly $20\times$ (for the 3-period CSS), were demonstrated, while achieving the same final relaxation state. When comparing control and CSS samples with intermediate thickness, more relaxation is observed for the CSS versus control at an equivalent TDD. As such, we conclude that the CSS structure provides enhanced dislocation glide, and thus reduced dislocation introduction, for n-GaP/Si, as opposed to conventional filtering effects.

Subsequent growth of n-type GaAs_yP_{1-y} SGBs on the 3-period CSS 500 nm n-GaP/Si virtual substrate was found to yield a nearly order of magnitude lower TDD (3×10^6 cm⁻² versus $\sim2\times10^7$ cm⁻²) at the terminal n-GaAs_{0.75}P_{0.25} than equivalent growths on non-CSS substrates. This TDD for n-GaAs_{0.75}P_{0.25} was even lower than equivalent metamorphic structures employing all p-type materials. While more investigation is needed to fully understand and optimize the TDD reduction mechanisms of the CSS, such structures appear to be promising candidates for the production of low-TDD, high-performance III-V/Si solar cells, as well as other integrated devices.

AUTHOR INFORMATION

Corresponding Author

*All correspondence should be sent to: grassman.5@osu

Author Contributions

The manuscript was written through contributions of all authors. All authors have given approval to the final version of the manuscript.

Funding Sources

National Science Foundation under Grant No. 1708957, Department of Energy, Office of Energy Efficiency and Renewable Energy (EERE), under Award Number DE-EE0007539.

Notes

Any additional relevant notes should be placed here.

ACKNOWLEDGMENT

This material is based upon work supported by the National Science Foundation under Grant No. 1708957, and by the Department of Energy, Office of Energy Efficiency and Renewable Energy (EERE), under Award Number DE-EE0007539. J.T.B was supported by a NASA Space Technology Research Fellowship (NNX16AM50H). A.N.B. and D.L.L. were supported by National Science Foundation Graduate Research Fellowships under Grant Nos. DGE-1343012 and DGE-1650114, respectively.

REFERENCES

- (1) Grassman, T. J.; Chmielewski, D. J.; Carnevale, S. D.; Carlin, J. A.; Ringel, S. A. GaAs_{0.75}P_{0.25}/Si Dual-Junction Solar Cells Grown by MBE and MOCVD. *IEEE J. Photovoltaics* **2016**, 6, 326–331. https://doi.org/10.1109/JPHOTOV.2015.2493365.
- (2) Grassman, T. J.; Derkacs, D.; Whipple, S. G.; Stavrides, A. P.; Bremner, S. P.; Ringel, S. A.; Lepkowski, D. L.; Boyer, J. T.; Chmielewski, D. J.; Yi, C.; Western, N.; Mehrvarz, H.; Ho-Baillie, A.; Kerestes, C. Toward >25% Efficient Monolithic Epitaxial GaAsP/Si Tandem Solar

Cells. In 2019 IEEE 46th Photovoltaic Specialists Conference (PVSC); IEEE, 2019; pp 0734–0737. https://doi.org/10.1109/PVSC40753.2019.8980574.

- (3) Fan, S.; Yu, Z. J.; Sun, Y.; Weigand, W.; Dhingra, P.; Kim, M.; Hool, R. D.; Ratta, E. D.; Holman, Z. C.; Lee, M. L. Solar Energy Materials and Solar Cells 20% Efficient Epitaxial GaAsP/Si Tandem Solar Cells. *Sol. Energy Mater. Sol. Cells* 2019, 202, 110144. https://doi.org/10.1016/j.solmat.2019.110144.
- (4) Feifel, M.; Lackner, D.; Ohlmann, J.; Benick, J.; Hermle, M.; Dimroth, F. Direct Growth of a GaInP/GaAs/Si Triple-Junction Solar Cell with 22.3% AM1.5G Efficiency. *Sol. RRL* **2019**, 3, 1900313. https://doi.org/10.1002/solr.201900313.
- (5) Takagi, Y.; Yonezu, H.; Samonji, K.; Tsuji, T.; Ohshima, N. Generation and Suppression Process of Crystalline Defects in GaP Layers Grown on Misoriented Si(100) Substrates. *J. Cryst. Growth* **1998**, 187, 42–50. https://doi.org/10.1016/S0022-0248(97)00862-2.
- (6) Grassman, T. J.; Carlin, J. A.; Galiana, B.; Yang, L. M.; Yang, F.; Mills, M. J.; Ringel, S. A. Nucleation-Related Defect-Free GaP/Si(100) Heteroepitaxy via Metal-Organic Chemical Vapor Deposition. *Appl. Phys. Lett.* **2013**, 102, 17–21. https://doi.org/10.1063/1.4801498.
- (7) Volz, K.; Beyer, A.; Witte, W.; Ohlmann, J.; Nmeth, I.; Kunert, B.; Stolz, W. GaP-Nucleation on Exact Si (0 0 1) Substrates for III/V Device Integration. *J. Cryst. Growth* **2011**, 315, 37–47. https://doi.org/10.1016/j.jcrysgro.2010.10.036.
- (8) Warren, E. L.; Kibbler, A. E.; France, R. M.; Norman, A. G.; Stradins, P.; McMahon, W. E. Growth of Antiphase-Domain-Free GaP on Si Substrates by Metalorganic Chemical Vapor Deposition Using an *in situ* AsH₃ Surface Preparation. *Appl. Phys. Lett.* **2015**, 107, 082109. https://doi.org/10.1063/1.4929714.
 - (9) Yamaguchi, M.; Amano, C. Efficiency Calculations of Thin-Film GaAs Solar Cells on Si

Substrates. J. Appl. Phys. 1985, 58, 3601–3606. https://doi.org/10.1063/1.335737.

- (10) Andre, C. L.; Boeckl, J. J.; Wilt, D. M.; Pitera, A. J.; Lee, M. L.; Fitzgerald, E. A.; Keyes, B. M.; Ringel, S. A. Impact of Dislocations on Minority Carrier Electron and Hole Lifetimes in GaAs Grown on Metamorphic SiGe Substrates. *Appl. Phys. Lett.* **2004**, 84, 3447–3449. https://doi.org/10.1063/1.1736318.
- (11) Boyer, J. T.; Lepkowski, D. L.; Chmielewski, D. J.; Derkacs, D.; Kerestes, C.; Stavrides, A.; Whipple, S.; Ringel, S. A.; Grassman, T. J. Development and Characterization of III-V/Si Multijunction Photovoltaics for Space Application. In *2019 IEEE 46th Photovoltaic Specialists Conference* (*PVSC*); IEEE, 2019; pp 2822–2825. https://doi.org/10.1109/PVSC40753.2019.8980737.
- (12) Yaung, K. N.; Vaisman, M.; Lang, J.; Lee, M. L. GaAsP Solar Cells on GaP/Si with Low Threading Dislocation Density. *Appl. Phys. Lett.* **2016**, 109, 032107. https://doi.org/10.1063/1.4959825.
- (13) Hool, R. D.; Chai, Y.; Sun, Y.; Eng, B. C.; Dhingra, P.; Fan, S.; Nay Yaung, K.; Lee, M. L. Relaxed GaP on Si with Low Threading Dislocation Density. *Appl. Phys. Lett.* **2020**, 116. https://doi.org/10.1063/1.5141122.
- (14) Sakata, I.; Kawanami, H. Band Discontinuities in Gallium Phosphide/Crystalline Silicon Heterojunctions Studied by Internal Photoemission. *Appl. Phys. Express* **2008**, 1, 0912011–0912013. https://doi.org/10.1143/APEX.1.091201.
- (15) Grassman, T. J.; Carlin, J. A.; Galiana, B.; Yang, F.; Mills, M. J.; Ringel, S. A. MOCVD-Grown GaP / Si Subcells for Integrated. *IEEE J. Photovoltaics* **2014**, 4, 972–980.
- (16) Yonenaga, I. Mechanical Properties and Dislocation Dynamics in III-V Compounds. *J. Phys. III* **1997**, 7, 1435–1450. https://doi.org/10.1051/jp3:1997198.

- (17) Yonenaga, I.; Sumino, K. Dynamic Activity of Dislocations in Gallium Phosphide. *J. Appl. Phys.* **1993**, 73, 1681–1685. https://doi.org/10.1063/1.353203.
- (18) Okamoto, H.; Watanabe, Y.; Kadota, Y.; Ohmachi, Y. Dislocation Reduction in GaAs on Si by Thermal Cycles and InGaAs/GaAs Strained-Layer Superlattices. *Jpn. J. Appl. Phys.* **1987**, 26, L1950–L1952. https://doi.org/10.1143/JJAP.26.L1950.
- (19) Takano, Y.; Hisaka, M.; Fujii, N.; Suzuki, K.; Kuwahara, K.; Fuke, S. Reduction of Threading Dislocations by InGaAs Interlayer in GaAs Layers Grown on Si Substrates. *Appl. Phys. Lett.* **1998**, 73, 2917–2919. https://doi.org/10.1063/1.122629.
- (20) Romanov, A. E.; Pompe, W.; Mathis, S.; Beltz, G. E.; Speck, J. S. Threading Dislocation Reduction in Strained Layers. *J. Appl. Phys.* **1999**, 85, 182–192. https://doi.org/10.1063/1.369467.
- (21) Speck, J. S.; Brewer, M. A.; Beltz, G.; Romanov, A. E.; Pompe, W. Scaling Laws for the Reduction of Threading Dislocation Densities in Homogeneous Buffer Layers. *J. Appl. Phys.* **1996**, 80, 3808–3816. https://doi.org/10.1063/1.363334.
- (22) George, I.; Becagli, F.; Liu, H. Y.; Wu, J.; Tang, M.; Beanland, R. Dislocation Filters in GaAs on Si. *Semicond. Sci. Technol.* **2015**, 30. https://doi.org/10.1088/0268-1242/30/11/114004.
- (23) Radzimski, Z. J.; Jiang, B. L.; Rozgonyi, G. A.; Humphreys, T. P.; Hamaguchi, N.; Parker, C.; Bedair, S. M. Misfit Stress Relaxation Phenomena in GaAsP-InGaAs Strained-Layer Superlattices. *Appl. Phys. Lett.* **1988**, 52, 1692–1694. https://doi.org/10.1063/1.99638.
- (24) Matthews, J. W.; Blakeslee, A. E.; Mader, S. Use of Misfit Strain to Remove Dislocations from Epitaxial Thin Films. *Thin Solid Films* **1976**, 33, 253–266. https://doi.org/10.1016/0040-6090(76)90085-7.
- (25) Carnevale, S. D.; Deitz, J. I.; Carlin, J. A.; Picard, Y. N.; De Graef, M.; Ringel, S. A.; Grassman, T. J. Rapid Misfit Dislocation Characterization in Heteroepitaxial III-V/Si Thin Films

- by Electron Channeling Contrast Imaging. *Appl. Phys. Lett.* **2014**, 104, 232111. https://doi.org/10.1063/1.4883371.
- (26) Klinger, V.; Roesener, T.; Lorenz, G.; Petzold, M.; Dimroth, F. Determination of Hardness and Young's Modulus for Important III-V Compound Semiconductors. *Thin Solid Films* **2013**, 548, 358–365. https://doi.org/10.1016/j.tsf.2013.08.079.
- (27) Yonenaga, I.; Sumino, K.; Izawa, G.; Watanabe, H.; Matsui, J. Mechanical Property and Dislocation Dynamics of GaAsP Alloy Semiconductor. *J. Mater. Res.* **1989**, 4, 361–365. https://doi.org/10.1557/JMR.1989.0361.
- (28) Yonenaga, I. Hardness, Yield Strength, and Dislocation Velocity in Elemental and Compound Semiconductors. *Mater. Trans.* **2005**, 46, 1979–1985. https://doi.org/10.2320/matertrans.46.1979.
- (29) Deitz, J. I.; Carnevale, S. D.; Ringel, S. A.; McComb, D. W.; Grassman, T. J. Electron Channeling Contrast Imaging for Rapid III-V Heteroepitaxial Characterization. *J. Vis. Exp.* **2015**, 2015, 1–8. https://doi.org/10.3791/52745.
- (30) Carnevale, S. D.; Deitz, J. I.; Carlin, J. A.; Picard, Y. N.; McComb, D. W.; De Graef, M.; Ringel, S. A.; Grassman, T. J. Applications of Electron Channeling Contrast Imaging for the Rapid Characterization of Extended Defects in III-V/Si Heterostructures. *IEEE J. Photovoltaics* **2015**, 5, 676–682. https://doi.org/10.1109/JPHOTOV.2014.2379111.
- (31) Blumer, A. N.; Boyer, J. T.; Deitz, J. I.; Rodriguez, F. A.; Grassman, T. J. Quantitative Characterization of Misfit Dislocations at GaP/Si Heteroepitaxial Interfaces via Electron Channeling Contrast Imaging and Semi-Automated Image Analysis. *Microsc. Microanal.* **2019**, 25, 202–203. https://doi.org/10.1017/S1431927619001740.
 - (32) Wilkinson, A. J.; Hirsch, P. B. Electron Diffraction Based Techniques in Scanning Electron

Microscopy of Bulk Materials. 1997, 4328.

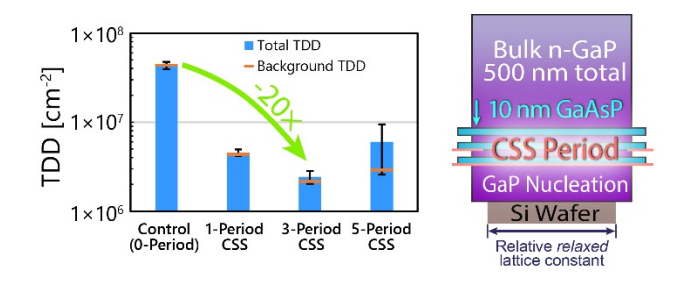
- (33) Wilkinson, A. J. Observation of Strain Distributions in Partially Relaxed In_{0.2}Ga_{0.8}As on GaAs Using Electron Channelling Contrast Imaging. *Philos. Mag. Lett.* **1996**, 73, 337–344. https://doi.org/10.1080/095008396180605.
- (34) Matthews, J. W.; Mader, S.; Light, T. B. Accommodation of Misfit across the Interface between Crystals of Semiconducting Elements or Compounds. *J. Appl. Phys.* **1970**, 41, 3800–3804. https://doi.org/10.1063/1.1659510.
- (35) Beanland, R. Multiplication of Misfit Dislocations in Epitaxial Layers. *J. Appl. Phys.* **1992**, 72, 4031–4035. https://doi.org/10.1063/1.352257.
- (36) Roesener, T.; Klinger, V.; Weuffen, C.; Lackner, D.; Dimroth, F. Determination of Heteroepitaxial Layer Relaxation at Growth Temperature from Room Temperature X-Ray Reciprocal Space Maps. *J. Cryst. Growth* **2013**, 368, 21–28. https://doi.org/10.1016/j.jcrysgro.2013.01.007.
- (37) Fitzgerald, E. A.; Watson, G. P.; Proano, R. E.; Ast, D. G.; Kirchner, P. D.; Pettit, G. D.; Woodall, J. M. Nucleation Mechanisms and the Elimination of Misfit Dislocations at Mismatched Interfaces by Reduction in Growth Area. *J. Appl. Phys.* **1989**, 65, 2220–2237. https://doi.org/10.1063/1.342834.
- (38) Fitzgerald, E. A.; Kim, A. Y.; Currie, M. T.; Langdo, T. A.; Taraschi, G.; Bulsara, M. T. Dislocation Dynamics in Relaxed Graded Composition Semiconductors. *Mater. Sci. Eng. B Solid-State Mater. Adv. Technol.* **1999**, 67, 53–61. https://doi.org/10.1016/S0921-5107(99)00209-3.
- (39) Onno, A.; Wu, J.; Jiang, Q.; Chen, S.; Tang, M.; Maidaniuk, Y.; Benamara, M.; Mazur, Y. I.; Salamo, G. J.; Harder, N. P.; Oberbeck, L.; Liu, H. Al_{0.2}Ga_{0.8}As Solar Cells Monolithically Grown on Si and GaAs by MBE for III-V/Si Tandem Dual-Junction Applications. *Energy*

Procedia 2016, 92, 661–668. https://doi.org/10.1016/j.egypro.2016.07.037.

"For Table of Contents Use Only"

Reduced Dislocation Introduction in III-V/Si Heterostructures with Glide-Enhancing Compressively-Strained Superlattices

Jacob T. Boyer, Ari N. Blumer, Zak H. Blumer, Daniel L. Lepkowski, and Tyler J. Grassman



The novel use of a $GaAs_yP_{1-y}/GaP$ compressively-strained superlattice (CSS) to enhance effective dislocation glide velocity in relaxed, 500 nm thick, n-type GaP/Si virtual substrates is demonstrated. A nearly $20\times$ relative TDD reduction (to $2.4\pm0.4\times10^6$ cm⁻²) with a 3-period CSS structure is achieved, enabling $GaAs_{0.75}P_{0.25}$ material for III-V/Si 2J solar cells with $3.0\pm0.6\times10^6$ cm⁻² TDD.